Applied Thermal Engineering 298 (2026) 130933

Contents lists available at ScienceDirect

Applied Thermal Engineering

journal homepage: www.elsevier.com/locate/apthermeng

Research Paper

All-weather passive building thermal management: Design and performance evaluation of radiative cooling coating integrated with phase change materials

Hengkang He [a], Qingyun Zhao [a], Bozhong Chen [a], Zhaoli Zhang [a], Nan Zhang [a,*], Shady Attia [b], Yanping Yuan [a], Jerzy Wołoszyn [c]

[a] School of Mechanical Engineering, Southwest Jiaotong University, Chengdu, China
[b] Sustainable Building Design Lab, Department UEE, Applied Sciences, University of Liège, Belgium
[c] Faculty of Mechanical Engineering and Robotics, AGH University of Krakow, Poland

ARTICLE INFO

Keywords:
Radiative cooling
Phase change material
Multilayer structure
Thermal buffering
Building thermal management

ABSTRACT

Radiative cooling (RC) offers a sustainable, energy-free solution to reduce reliance on traditional cooling systems in buildings. However, continuous radiative cooling can cause overcooling at night or during winter. To address this issue, phase change material (PCM) was integrated beneath RC. Paraffin, SiO_2 and h-BN were separately introduced into a homologous polydimethylsiloxane (PDMS) matrix to form a three-layer RCPCM film. The properties of the RCPCM film were comprehensively characterized. And the results show that RCPCM film has excellent optical performance, with a solar-weighted reflectance of 0.93 and an atmospheric window emissivity of 0.94. Outdoor summer tests under a peak irradiance of 880 W/m^2 demonstrate that RCPCM achieves a maximum temperature reduction of 21 °C compared to a blank cavity and 7 °C relative to a commercial coating, with a radiative cooling power reaching 125 W/m^2. Winter tests further confirm its significant thermal buffering and anti-overcooling performance at night. EnergyPlus simulations indicate that applying RCPCM to building roofs substantially mitigates overcooling, with additional energy savings of up to 1.66 MJ/m^2 compared to commercial coatings. This study demonstrates that combining a spectrally selective radiative surface with latent heat thermal energy storage enables climate-adaptive, all-weather passive thermal management while delivering quantifiable annual energy savings.

1. Introduction

Rapid economic development has led to a sharp rise in energy consumption and triggered a dual crisis of energy shortage and environmental pollution. Global warming and frequent extreme hot weather events caused by this not only threaten human health, but also increase the cooling energy consumption of buildings [1,2]. In this context, the development of green and sustainable refrigeration technologies has evolved into one of the key routes to alleviate building energy consumption and improve thermal comfort [3–6].

As a new type of energy-efficient refrigeration technology, Passive daytime radiative cooling (PDRC) technology is a novel energy-free refrigeration technology that can release heat directly into space by reflecting solar radiation within the solar band (0.2–2.5 μm) and emitting infrared energy within the atmospheric window band (8–13 μm) [7–10]. Its advantages of environmental-friendly, low energy consumption, simple utilization guarantee it to extensively apply in building energy conservation [11,12], human thermal management [13,14], solar cell cooling [15,16], etc. Polymer-based PDRC materials including polyvinylidene fluoride-hexafluoropropylene (PVDF-HFP), polymethyl methacrylate (PMMA), modified epoxy resins, thermoplastic polyurethane (TPU), and polydimethylsiloxane (PDMS) have attracted much attention due to their low cost, easy processing and excellent spectral selectivity. Among them, PDMS featured with a especial infrared absorption peak at 9.5 μm is growing into one of the promising candidates for PRC application [17–20]. Whereas, the instinct high transmittance of PDMS largely restricts its practical employments. Thus, incorporating nanoparticles into PDMS as refractive media is an effective way to improve the reflectivity. Common refractive media including zirconium oxide (ZrO_2) [20,21], titanium oxide (TiO_2) [22,23], aluminum oxide (Al_2O_3) [24], silicon oxide (SiO_2) [25–27], and boron nitride (BN) [28–30], etc. have been introduced to the PDMS substrate.

* Corresponding author.

https://doi.org/10.1016/j.applthermaleng.2026.130933
Received 1 December 2025; Received in revised form 2 April 2026; Accepted 6 April 2026
Available online 7 April 2026

Actually, BN is widely used in RC due to the high thermal conductivity and high refractive index. However, available studies have shown that an excessively high content of BN can be detrimental. Its high refractive index in the mid-infrared region limits the mid-infrared emissivity of the coating [31,32]. To address this issue, BN can be combined with other particles through a hierarchically structural design to improve its IR emissivity while maintaining its high solar reflectance. Satoshi et al. [31] prepared a two-layer radiation-cooled layer, which compensated for the lack of emissivity of BN by adding an additional layer of SiO_2, and the coating had an average solar reflectivity of up to 99% and an average emissivity of 93%. Wang et al. [33] incorporated BN into a PDMS matrix and fabricated a single-layer radiative-cooling film in which BN is embedded and fluoride-modified $BaSO_4$ is randomly semi-embedded, achieving an average reflectance of 94.73% and an average emissivity of 95.96%.

However, the effect of RC on the object or building fails under high-temperature environment, consistently increasing the temperature of the object or building until a new thermal equilibrium. To address this issue, a new strategy integrating RC material with phase change materials (PCMs) has been proposed to manage high-temperature thermal shocks [34,35]. PCMs can absorb and release heat isothermally during their melting and solidification processes. Owing to the advantages of high energy density and low temperature fluctuations, they are widely used in thermal management applications for buildings, human bodies, and electronic devices [36–39]. Meng et al. [40] designed a bilayer structure integrating porous fibers and PCMs to regulate the heat transfer between the environment and the building. Qin et al. [41] developed a design combining RC and PCM latent heat to achieve 39 °C cooling under thermal shock. Wang et al. [42] fabricated a phase change composite membrane (PCCF) with 24-h cold energy management, which provided 180 W/m^2 cooling power and 11.95 °C cooling effect through cosmic cold harvesting. Tao et al. [43] constructed a PCM@NF@SRCF by dodecanol impregnated nickel foam. PCM@NF@SRCE bilayer membrane improved the cooling effect by 1–2 °C in sunlight and the thermal buffering effect by 2–3 °C in cold conditions. Based on the above review, RCPCM aims to deliver—in a single building envelope—high solar reflectance, high emissivity in the atmospheric window, and low-thermal-resistance coupling between layers. It also seeks to match phase-change behavior to diurnal and seasonal loads. In practice, these targets are difficult to achieve simultaneously. Optical-thermal trade-offs, weak interlayer adhesion and thermal contact, and phase-change hysteresis constrain performance. Additional challenges include limited net cooling power, immature manufacturability and scale-up, and insufficient evidence on regional applicability.

Based on this, we integrated PCM beneath the radiative cooling layer using an in-situ growth and integrated fabrication process, developing a three-layer RCPCM film by incorporating PW with a phase change temperature of 28–32 °C [44,45], SiO_2, and h-BN into a homologous PDMS matrix. Specifically, the incorporation of h-BN provides high reflectance to reduce solar heat gain, while SiO_2 is introduced to optimize the material's emissivity and enhance its thermal insulation properties, enabling h-BN and SiO_2 to synergistically regulate radiative cooling performance. The PDMS/PW phase-change layer serves as a phase-change buffer unit, absorbing and storing excess thermal energy from the radiative cooling layer during the day and releasing the stored energy at night, thereby mitigating environmental temperature fluctuations and thermal shock. Compared to post-bonding or simple stacking processes, in-situ growth significantly improves interlayer adhesion, effectively avoiding delamination risks and thus enhancing structural integrity and reliability. In addition, the continuous PDMS matrix across the three-layer structure helps reduce interfacial thermal resistance. It promotes efficient heat transfer between the radiative cooling layer and the PCM layer. As a result, it strengthens daytime energy absorption and storage. It also enhances nighttime heat release and thermal buffering. This effect improves the overall thermal management performance of the RCPCM.

2. Material preparation and characterization

2.1. Experimental materials and instruments

The basic information of experimental materials used in this study are listed in Table 1, and the experimental instruments are provided in Table 2.

2.2. Material preparation

The RCPCM was designed as a three-layer structure consisting of a top PDMS/h-BN layer, a middle PDMS/SiO_2 layer, and a bottom PDMS/PW phase-change layer. The specific preparation procedure is shown in Fig. 1.

Step 1: The PDMS elastomer precursor A and Sylgard 184 silicone curing agent B were mixed with ethyl acetate solution at a mass ratio of 10:1:5. A specific amount of h-BN was then added to the mixture, which was stirred with a magnetic stirrer for 30 min to ensure uniform dispersion. The resulting solution was poured into a mold and left it at room temperature for 20 min to eliminate bubbles and self-level under gravity. It was then placed in an electric blast drying oven at 50 °C for 2 h to cure, forming a semi-cured PDMS/h-BN film.

Step 2: Similar to the procedure in Step 1. The h-BN in the process was replaced with ball-milled SiO_2, and the resulting mixture was poured onto the semi-cured PDMS/h-BN film, then placed in a 50 °C constant-temperature oven to cure for 2 h, thereby obtaining a semi-cured PDMS/h-BN–PDMS/SiO_2 film.

Step 3: A specific amount of PW was weighed into a beaker and heated until completely melted. After melting, PDMS (with a base-to-curing agent ratio of 10:1) was added to the molten PW. The beaker was placed in a 50 °C water bath and stirred at 400 rpm for 30 min to ensure thorough mixing. The mixture was then poured onto the semi-cured PDMS/h-BN–PDMS/SiO_2 bilayer film. It was subsequently cured at 50 °C for 5 h in a forced-air drying oven. Finally, the sample was demolded and flipped to obtain the complete RCPCM composite.

To investigate the effects of SiO_2 content, the thickness ratio of the radiative cooling layer, and the thickness of the phase-change layer on cooling performance, we prepared a series of films with varying parameters. Specifically, films with different SiO_2 contents (5 wt%, 10 wt %, 15 wt%, and 20 wt%) were fabricated. Furthermore, the thickness ratio of the radiative cooling layer was adjusted to 0:2, 0.5:1.5, 1:1, 1.5:0.5, and 2:0, while maintaining a constant total thickness of 2 mm. Additionally, films with PCM thicknesses of 2 mm, 4 mm, 6 mm, and 8 mm were also prepared. We named these samples as RCPCM-X-Y, where X and Y represent the thickness of the PDMS/SiO_2 layer and the SiO_2 content in that layer. The parameters of the prepared samples are shown

Table 1
Detailed list of experimental materials.

Material (Abbreviation)	Specification	Manufacturer
Hexagonal boron nitride (h-BN)	Particle size: 500 nm; Purity: ≥ 99.9%	Muheng Metal Materials Co., Ltd
Nano-sized silicon dioxide (SiO_2)	Particle size: 30 nm; Purity: ≥ 99.9%	Muheng Metal Materials Co., Ltd
Ethyl acetate (EA)	Purity: ≥99.5%	Chengdu Kelong Chemical Co., Ltd
Paraffin wax (PW)	Phase-change temperature: 32 °C; Purity: ≥ 99%	Guangzhou Zhongjia New Material Technology Co., Ltd
Polydimethylsiloxane (PDMS)	Transparent viscous liquid	Changan Xinke New Materials Business Department
Commercial coatings	White viscous liquid; Average reflectance: 0.84; Average emissivity: 0.91; Thickness: 2 mm	Guangzhou Fumei'ao Coatings Co., Ltd.

Table 2
Detailed list of experimental instruments.

Instrument	Model	Manufacturer
Electric blast drying oven	101-OS	Shanghai Lichen Bangxi Instrument Technology Co., Ltd
Constant temperature water bath	DF-101S	Shanghai Lichen Bangxi Instrument Technology Co., Ltd
Vertical semi-circular ball mill	XQM-0.4	Changsha Tencan Powder Technology Co., Ltd.

in Table 3.

2.3. Material characterization

Topography characterization: The microscopic surface and cross-section microstructure of RCPCM were observed by scanning electron microscopy (SEM, Sigma 500, ZEISS, Germany).

Thermal storage performance test:The PDMS/PW was tested by differential scanning calorimetry (DSC, TAQ20, USA), and the temperature range was 0–60 °C under N_2 atmosphere, with a rise and cooling rate of 5 °C/min.

Hydrophobic performance test:The static water contact angle (WCA) was determined at room temperature by adding 25 μL of deionized water dropwise to the surface of the film using an optical contact angle measuring instrument (SINDIN, SDC100, China). Each sample is measured at 5 different locations, with the maximum value as the final measurement result.

Thermal conductivity test:Each layer of the material was tested by using a thermal conductivity meter (TC3100, China), and the samples were prepared into 5.5 mm × 5.5 mm × 1 mm (length × width × height) sheets, placed on the sensor, the test voltage was 2 V, and each sample was tested 5 times at room temperature, and the results were averaged.

Reflectance spectroscopy: In diffuse reflection mode, UV-VIS-NIR reflectance spectra in the wavelength range of 250–2500 nm were recorded using a UV-VIS-NIR spectrophotometer (U-4100, Hitachi, Japan) equipped with an integrating sphere attachment.

Absorption spectroscopy: Absorption spectra in the MIR range (2.5–25 μm) were recorded using a Fourier transform infrared (FTIR) spectrometer (Thermo-Fisher Scientific Instrument Nicolet IS50FTIR) coupled to a MIR integrating sphere in diffuse reflection mode.

2.4. Radiant cooling power calculation

Average solar reflectance $\overline{R}_{solar}$ and average emissivity $\overline{\varepsilon}_{LWIR}$ are defined within the long-wave infrared atmospheric transparency window (8–13 μm) as follows [46]:

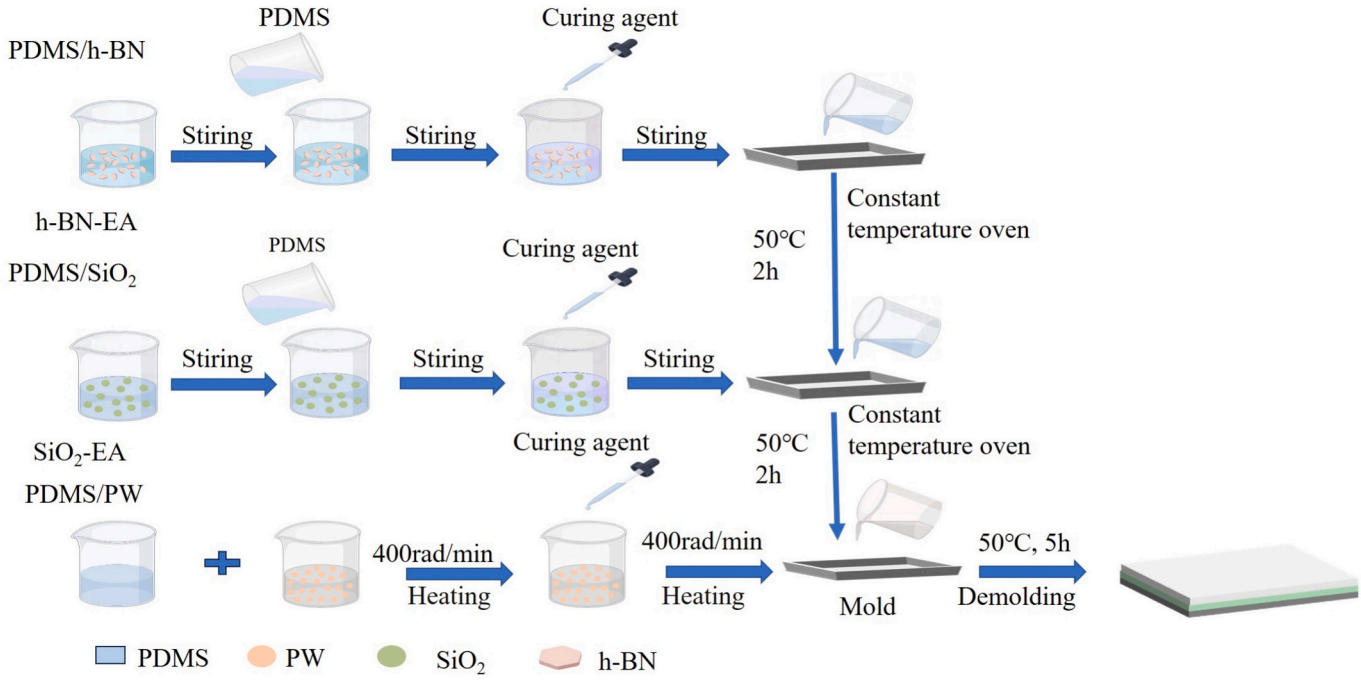

Fig. 1. Flow chart of RCPCM material preparation.

Table 3
Composition and specifications of obtained RCPCMs.

RCPCM	PDMS/h-BN		PDMS/SiO_2		PDMS/PW	
	Content	Thickness(mm)	Content	Thickness(mm)	Content	Thickness(mm)
RCPCM-2-10	30%	0	10%	2	30%	4
RCPCM-1.5-10	30%	0.5	10%	1.5	30%	4
RCPCM-1-10	30%	1	10%	1	30%	4
RCPCM-0.5-10	30%	1.5	10%	0.5	30%	4
RCPCM-0-10	30%	2	10%	0	30%	4
RCPCM-0.5-5	30%	1.5	5%	0.5	30%	4
RCPCM-0.5-15	30%	1.5	15%	0.5	30%	4
RCPCM-0.5-20	30%	1.5	20%	0.5	30%	4

$$\overline{R}_{solar} = \frac{\int_{0.3\mu m}^{2.5\mu m} I_{solar}(\lambda) \times R_{solar}(\lambda,\theta)d\lambda}{\int_{0.3\mu m}^{2.5\mu m} I_{solar}(\lambda)d\lambda} \quad (1)$$

where λ is the wavelength of incident light in the range of 0.3–2.5 μm, I_{solar} is the solar intensity spectrum, and R_{solar} is the angular spectral reflectance of the surface.

$$\overline{\varepsilon}_{LWIR} = \frac{\int_{8\mu m}^{13\mu m} I_{BB}(\lambda) \times \varepsilon_{LWIR}(\lambda,\theta)d\lambda}{\int_{8\mu m}^{13\mu m} I_{BB}(\lambda)d\lambda} \quad (2)$$

where $I_{BB}(\lambda)$ is the spectral intensity of the blackbody emission, and $\varepsilon_{LWIR}(\lambda,\theta)$ is the angular spectral thermal emissivity of the surface in the range of 8–13 μm.

Theoretically, the cooling power of a horizontal surface directly facing the daytime sky P_{cool} equals the difference between the power e radiated outward by the surface at temperature T_s and the sum of the powers absorbed by the surface, as shown in Fig. 2. The absorbed powers include the incident downward atmospheric thermal radiation P_{atm}, the incident solar power P_{sun}, and the power lost due to convection and conduction $P_{cond+conv}$. The calculation formula is as follows [30,46]:

$$P_{cool} = P_{rad} - (P_{atm} + P_{sun} + P_{cond+conv}) \quad (3)$$

The difference between P_{rad} and P_{atm} is the net power emitted by the surface in the form of infrared radiation, which scales as the difference between the fourth power of absolute surface temperature minus the fourth power of absolute effective sky temperature T_{sky} [30,47].

$$P_{rad} - P_{atm} = \varepsilon\sigma\left(T_s^4 - T_{sky}^4\right) \quad (4)$$

where ε and σ are the overall infrared emissivity of the surface and the Stefan–Boltzmann constant (5.67×10^{-8} W·m^{-2}·K^{-4}), respectively. The incident downwelling atmospheric thermal radiation power P_{DLR} can be directly measured using a pyrgeometer. Therefore, Eq. (4) can be rewritten as [30,47]:

$$P_{rad} - P_{atm} = \varepsilon\sigma T_s^4 - \varepsilon P_{DLR} \quad (5)$$

For an opaque surface with a solar reflectance of R, the absorbed solar energy is [30,47]:

$$P_{sun} = (1-R)I \quad (6)$$

where I is the incident solar irradiance, which can be measured using a pyranometer.

The power lost due to conduction and convection, which is the sum of the conductive heat transfer due to the contact of the surface with the other external surfaces and the convective heat transfer owing to the contact of the surface with the adjacent air, is [30,47]:

$$P_{conv+cond} = h_{conv+cond}(T_{amb} - T_s) \quad (7)$$

Therefore eq. (3) can be rewritten as follows [30,47]:

$$P_{cool} = \varepsilon\sigma T_s^4 - \varepsilon P_{DLR} - (1-R)I - h_{conv+cond}(T_{amb} - T_s) \quad (8)$$

2.5. Performance tests

2.5.1. Performance testing of RCPCM under simulated solar irradiation

A xenon lamp (CEL—S500, CEAULIGHT, China) was employed to simulate solar radiation for the indoor simulated cooling test under natural heat dissipation conditions. The polystyrene (PS) foam is the thermal insulator. A square opening (6 cm × 6 cm × 1 cm) is created on the top side of the foam, where the RCPCM is placed inside. A K-type thermocouple connected to a data logger thermometer (34,970 A, Agilent, America) was placed under the RCPCM to measure the temperature at the bottom of the RCPCM.

2.5.2. Field RC performance of RCPCM

The RC performance of the samples was tested under outdoor practical conditions on a building roof in Chengdu. The weather stations (Vantage Pro2, Davis, America) were used to record wind speed, humidity, and solar irradiation. The RCPCM was positioned in the 10 cm × 10 cm × 1 cm cavity in the top of the PS foam (20 cm × 20 cm × 18 cm). The foam was covered with polyethylene film and highly reflective aluminum foil to minimize heat loss. Record the temperature at the bottom of the RCPCM.

2.5.3. Energy consumption simulation

To objectively evaluate the impact of applying PCPM to building envelopes on energy consumption, six representative Chinese cities were selected; their climatic characteristics and geographic distribution are shown in Fig. 3 and Table 4. Meteorological data for each city were obtained from the EnergyPlus weather database. RCPCM or a commercial coating was applied to the exterior surface of the roof, and energy-use simulations for each material configuration were conducted in EnergyPlus using the Conduction Finite Difference (CondFD) algorithm [48,49]. The building was modeled as an office building; the cooling season was set to June 1–August 31, and the heating seasons to January 1–March 15 and November 15–December 31. The air-conditioning system operated from 07:00 to 22:00 on weekdays with set-point temperatures of 24 °C (cooling) and 18 °C (heating).

In the energy simulation of building envelopes using radiative-cooling-coupled phase-change materials, this study adopted a modeling approach based on the unified control equations in EnergyPlus for the zone, envelope, and HVAC system. The simulation assumptions are as follows:

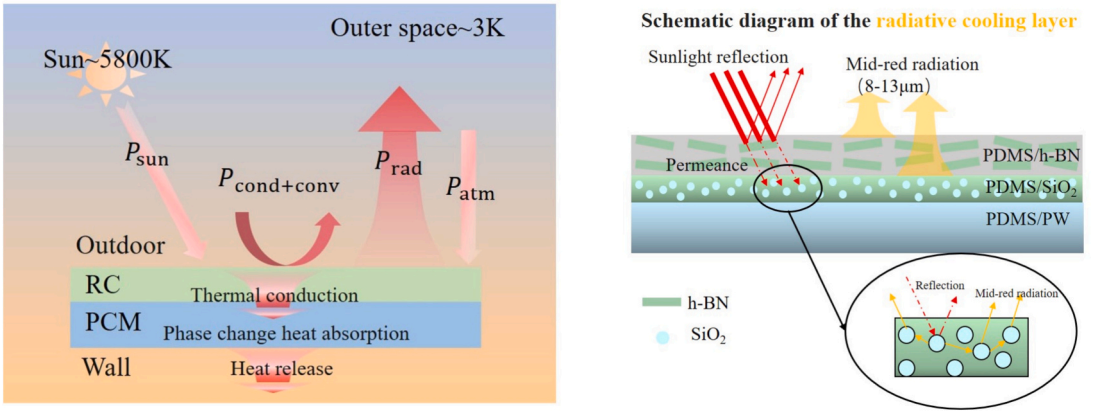

Fig. 2. Energy balance diagram of radiative cooling.

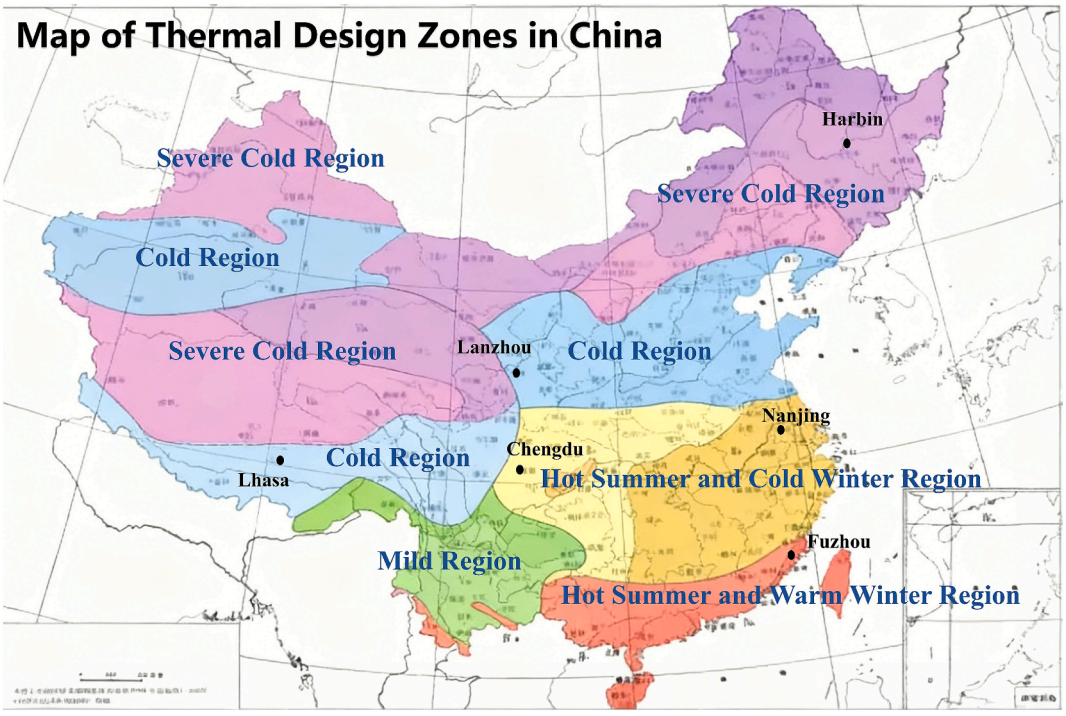

Fig. 3. Map of thermal design zones in China.

Table 4
Regional Characteristics of typical cities in various thermal design zones.

City	Cold zoning	Regional characteristics
Chengdu	Hot in summer and cold in winter	Subtropical humid monsoon climate with high rainfall and limited sunshine, featuring high summer cooling loads and noticeable winter heating demand.
Lhasa	Severe cold areas	Plateau temperate semi-arid climate with high elevation, low pressure, large diurnal temperature range, and strong solar radiation. Low annual temperatures lead to high heating demand and minimal summer cooling load.
Fuzhou	Hot in summer and warm in winter	Subtropical oceanic monsoon climate with warm, humid conditions year-round. Summers are hot and wet with high cooling loads, while winters are mild with minimal heating demand.
Nanjing	Hot in summer and cold in winter	Subtropical monsoon climate with hot, humid summers and cold winters. Abundant rainfall results in significant cooling and heating loads, making it a typical city with dual seasonal demand.
Lanzhou	Cold areas	Temperate continental climate with low rainfall, dry air, and strong solar radiation. Long, cold winters drive high heating demand, while short, hot summers result in low cooling loads.
Harbin	Severe cold areas	Temperate continental monsoon climate with long, extremely cold winters and high heating demand, while short, cool summers result in minimal cooling loads.

(1) The air in each thermal zone is fully mixed and uniform. For conditioned zones, the air temperature is determined by a lumped-parameter energy balance eq.
(2) Heat transfer through the envelope is modeled as one-dimensional conduction. Material thermophysical properties are treated as constant input values. The effects of thermal bridges and moisture transfer are assumed negligible or already represented in an equivalent manner.
(3) For the PCM layer, an effective heat-capacity model in enthalpy–temperature form is introduced. The model dynamically updates the equivalent specific heat and thermal conductivity using the enthalpy–temperature curve. This approach explicitly captures latent heat absorption and release, as well as the nonlinear evolution of the temperature field.
(4) Temperature and humidity set points, as well as on/off control, follow schedule-based control. The control is assumed ideal, and occupants are assumed not to change set points frequently.
(5) Non-ideal factors such as equipment aging and failure, construction defects, and microclimate effects are not considered.
(6) The HVAC system is simulated using Ideal Loads. The system type and the associated performance curves and efficiency parameters are assumed applicable under the target operating conditions.

2.6. Uncertainty analysis

Considering the inevitable errors caused by experimental conditions and environmental factors, the uncertainties of the main variables and parameters in the experiments were analyzed. The uncertainty values of the main variables are summarized in Table 5.

3. Results and discussion

3.1. Structure and morphology of RCPCM

3.1.1. Thermophysical properties of RCPCM

To characterize the thermal performance of PDMS/PW, we measured

Table 5
Uncertainty of the main experimental variables.

Variables	Uncertainty(%)
Temperature	1
Solar irradiance	2.89
Wind speed	2.89
Humidity	1.15
Xenon lamp	0.28

its enthalpy. The results are shown in Fig. 4 and Table 6. Compared to pure paraffin, the phase-change temperature of the PDMS/PW composite increases slightly, from 28.1 °C to 28.9 °C. This is mainly attributed to the heterogeneous nucleation effect of PDMS, which improves the crystallization quality of paraffin, while the interfacial interaction enhances the thermodynamic stability of the crystal. The melting latent heat of the PDMS/PW composite is 44.1 J/g, while that of pure paraffin is 164.1 J/g. The ratio between the latent heat of the composite and that of pure paraffin is basically consistent with the mass fraction of paraffin in the composite. This suggests that PDMS mainly serves as an encapsulation matrix and provides shape stability. PDMS/PW doesn't show obvious phase-change degradation or phase separation.

To evaluate the stability of RCPCM, we carried out a leakage test and a thermal cycling test on the PCM. The results are shown in Fig. 5. Fig. 5 (a, b) present the leakage test of PDMS/PW and the corresponding mass fraction curves. The results show that PW was almost fully melted after 10 min. In contrast, PDMS/PW showed no obvious leakage during 20 min of heating. It lost only 6% of its mass. Most latent heat was retained. These results indicate that PDMS can effectively encapsulate PW. They also confirm good thermal stability and shape stability during heating. The DSC curves of PDMS/PW before and after 100 thermal cycles are shown in Fig. 5(c) and Table 7. The curves show similar melting and crystallization features. This suggests that the composite keeps a clear phase-change behavior after repeated heating and cooling. The phase-change temperatures changed only slightly. However, the latent heat decreased to some extent. The melting enthalpy decreased from 44.1 J/g to 39.9 J/g. The freezing enthalpy decreased from 44.4 J/g to 40.52 J/g. After 100 cycles, the enthalpy retention was about 90%. This indicates that PDMS/PW still provides effective latent heat thermal energy storage. Overall, these results demonstrate good cycling thermal stability of PDMS/PW.

3.1.2. Optical Properties of RCPCM

Fig. 6(a) shows the solar reflectance and atmospheric window emissivity curves of RCPCM with varying radiative-cooling layer thickness ratios. As can be seen from the Fig.6, the reflectivity of RCPCM increases first and then decreases with the increase of wavelength. The reflectance curves of RCPCM-0.5-10 and RCPCM-0-10 nearly coincide, but in the 200–600 nm band, the reflectivity of RCPCM-0.5-10 is slightly higher than that of RCPCM-0-10. At a wavelength of 800 nm, RCPCM-0.5-10 has the highest reflectivity of 0.97. The ultra-high UV reflectivity of RCPCM can solve the high temperature caused by UV light. On the contrary, at the wavelength of 2500 nm, the reflectivity of RCPCM is only about 0.3, and the reflectivity of RCPCM in the infrared band needs to be further improved. The overall average solar reflectance of RCPCM-0.5-10 is 0.93. In addition, the emissivity of RCPCM in the atmospheric window band changes relatively gently, and the difference between RCPCM samples in the atmospheric window band is also very small, and the curves almost coincide. The average emissivity of RCPCM-0.5-10 in the atmospheric window band is 0.94. Fig. 6(b) presents the solar reflectance and atmospheric window emissivity of RCPCM samples with varying SiO_2 contents. RCPCM-0.5-10 demonstrates the highest reflectance in the wavelength range of 200–1500 nm. The highest solar-weighted reflectance achieved in other samples is 0.92, which is slightly lower than that of RCPCM-0.5-10. The average atmospheric window emissivity of the other samples is 0.93, also marginally below the value of 0.94 recorded for RCPCM-0.5-10.

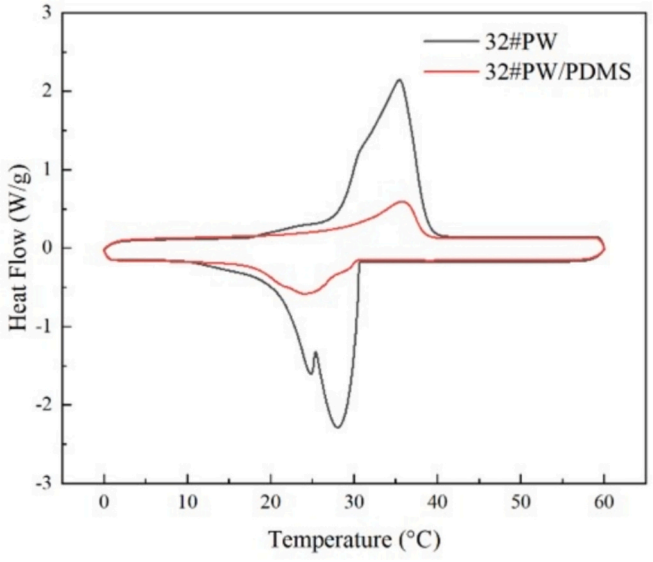

Fig. 4. DSC curve of PW and PDMS/PW.

Table 6
DSC results of phase change materials.

Sample	Melting process		Solidification process	
	Melting phase change temperature (°C)	Enthalpy of melting (J/g)	Solidification phase change temperature(°C)	Enthalpy of solidification (J/g)
PW	28.1	164.1	30.3	162.1
PDMS/PW	28.9	44.1	30.3	44.4

3.1.3. Structure and hydrophobic properties of RCPCM

As shown in Fig. 7(a), the RCPCM is a three-layer structure divided into two parts- the radiative-cooling layer and the phase-change layer. The radiative-cooling layer is composed of a PDMS/h-BN layer and a PDMS/SiO_2 layer with a total thickness of 2 mm. The h-BN-filled PDMS layer provides high solar reflectance, while the subsequent PDMS/SiO_2 layer plays a dual role in thermal insulation and emissivity regulation. Therefore, h-BN and SiO_2 synergistically enhance the radiative-cooling performance of RCPCM. The phase-change layer is PDMS/PW, which absorbs and stores the excess heat generated in the radiative-cooling layer during the daytime and releases the stored energy at night. As shown in Fig. 7(b), the cross-sectional SEM image further confirms the continuous multilayer architecture of RCPCM. The interfaces between the PDMS/h-BN, PDMS/SiO_2 and PDMS/PW layers are tightly bonded due to the in-situ growth process, and all three functional layers share PDMS as the matrix. This structural feature strengthens interlayer adhesion, reduces the interfacial thermal resistance, and improves the heat transfer efficiency during operation. Fig. 7(h) shows the SEM morphology of the PDMS/h-BN surface in RCPCM-0.5-10, indicating a relatively flat surface without obvious macroscopic defects. Fig.7(i) presents the water contact angle results of the PDMS/h-BN surface. All measured contact angles are higher than 90°, with an average value of 103.45°, demonstrating that RCPCM-0.5-10 possesses hydrophobic surface properties, which is beneficial for resisting moisture-related interference in practical outdoor use.

3.2. Performance of RCPCM under simulated solar irradiation

A xenon lamp was used as a solar simulator. The performance of RCPCM samples with different radiative-cooling layer thicknesses was tested under a constant irradiance. The experimental setup is shown in Fig. 8.

As shown in Fig. 9(b-e), the performance tests of RCPCM with varying radiative-cooling layer thickness ratios were carried out under irradiances of 800 W/m^2 and 1000 W/m^2. It can be seen that the temperature variation trend of each sample is basically consistent under constant irradiance, but the temperature level is obviously affected by the thickness distribution of the RC layer when the total thickness of the

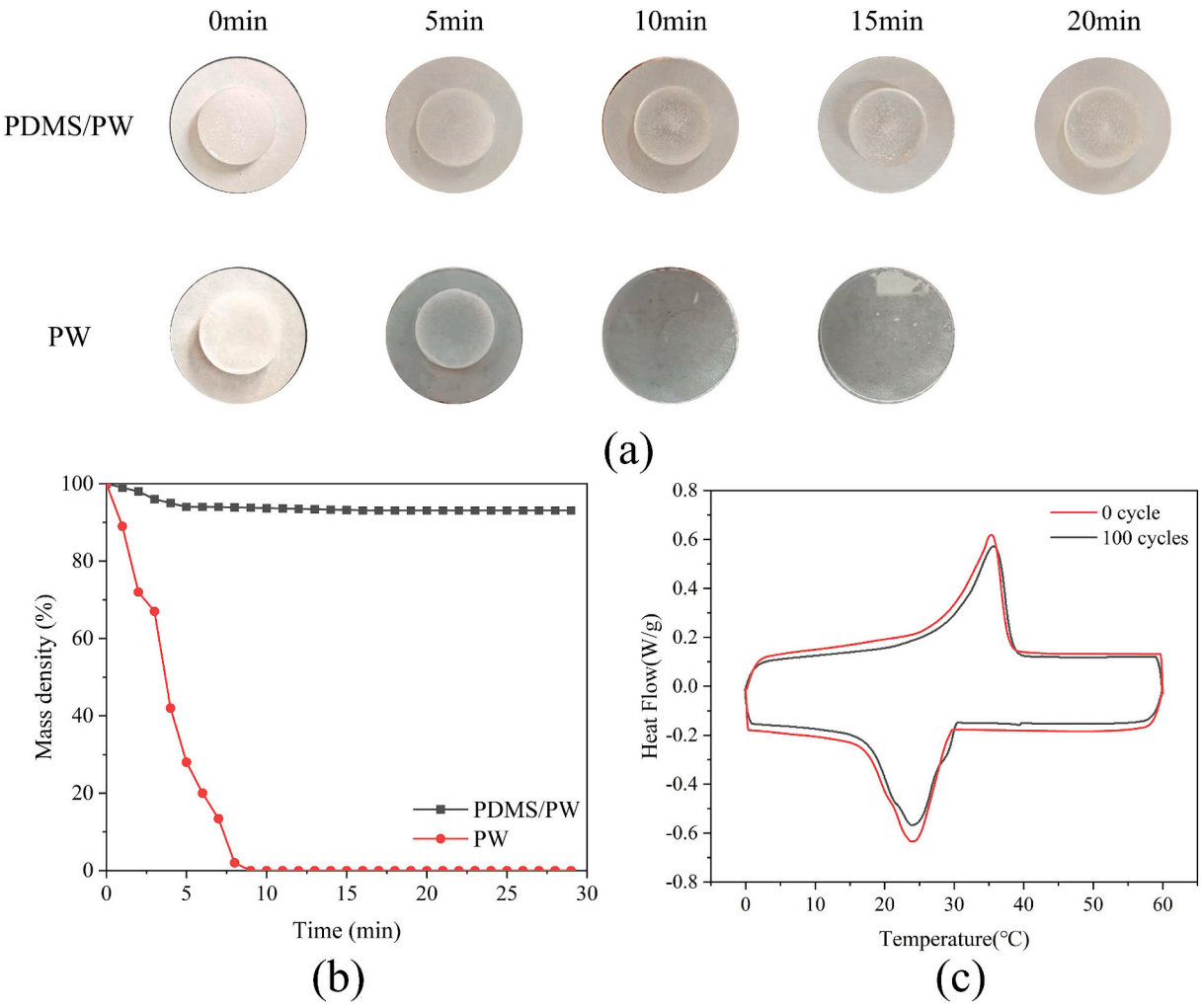

Fig. 5. Stability test results of PDMS/PW (a) Leakage tests of PDMS/PW and PW; (b) mass fraction curves of PDMS/PW and PW during the leakage tests; (c) DSC curves of PDMS/PW before and after 100 thermal cycles.

Table 7
DSC data of PDMS/PW before and after 100 thermal cycles.

Sample	Melting process		Solidification process	
	Melting phase change temperature(°C)	Enthalpy of melting (J/g)	Solidification phase change temperature(°C)	Enthalpy of solidification(J/g)
0 cycle	28.9	44.1	30.3	44.4
100 cycles	29	39.9	29.2	40.5

RC layer is fixed at 2 mm. Under both irradiances, the best RC performance is obtained by RCPCM-0.5-10, with maximum temperatures of 30 °C and 32 °C at 800 W/m^2 and 1000 W/m^2, respectively. This indicates that an appropriate thickness distribution of PDMS/h-BN and PDMS/SiO_2 can more effectively reduce solar heat gain and enhance radiative heat dissipation, thus lowering the quasi-steady temperature and improving the cooling advantage. In addition, after 3 h irradiation at 800 W/m^2, the temperatures of all RCPCM samples are around or below 32 °C, and even when the irradiance increases to 1000 W/m^2, RCPCM-0.5-10 and RCPCM-0-10 still remain below 32 °C, indicating that the optimized structure can adapt to high irradiance conditions in midsummer. In summary, when the total thickness of the RC layer is 2 mm, the configuration of PDMS/h-BN = 1.5 mm and PDMS/SiO_2 = 0.5 mm (RCPCM-0.5-10) exhibits the best radiative-cooling performance under both 800 and 1000 W/m^2.

At an irradiance of 800 W/m^2, the effect of SiO_2 content on RCPCM performance was evaluated (Fig. 9 f, g). RCPCM-0.5-5–20 correspond to 5%, 10%, 15%, and 20% SiO_2, respectively. As shown in Fig. 9 (f), the temperature of each sample increases with time and reaches a quasi-steady state at about 120–150 min. The commercial coating heats up fastest and attains the highest steady-state temperature, higher than all RCPCMs. Among all samples, RCPCM-0.5-10 exhibits the slowest heating rate and the lowest steady-state temperature. This ranking remains essentially unchanged over the whole test. Fig. 9 (g) presents the temperature difference relative to the commercial coating ($\Delta T = T_{RCPCM} - T_{Commercial}$). ΔT is negative for most of the test, indicating that the RCPCM surface temperatures remain lower than that of the commercial coating. RCPCM-0.5-10 shows the largest magnitude of negative ΔT and thus the strongest cooling advantage. RCPCM-0.5-5 and RCPCM-0.5-20 follow, and RCPCM-0.5-15 is the weakest. Overall, the SiO_2 content in the radiative-cooling layer affects performance, but higher content does not necessarily yield better cooling. Under the solar simulator, RCPCM-0.5-10 performs best. It can be seen that changing the SiO_2 loading will affect the optical–thermal balance of the radiative-cooling layer, and

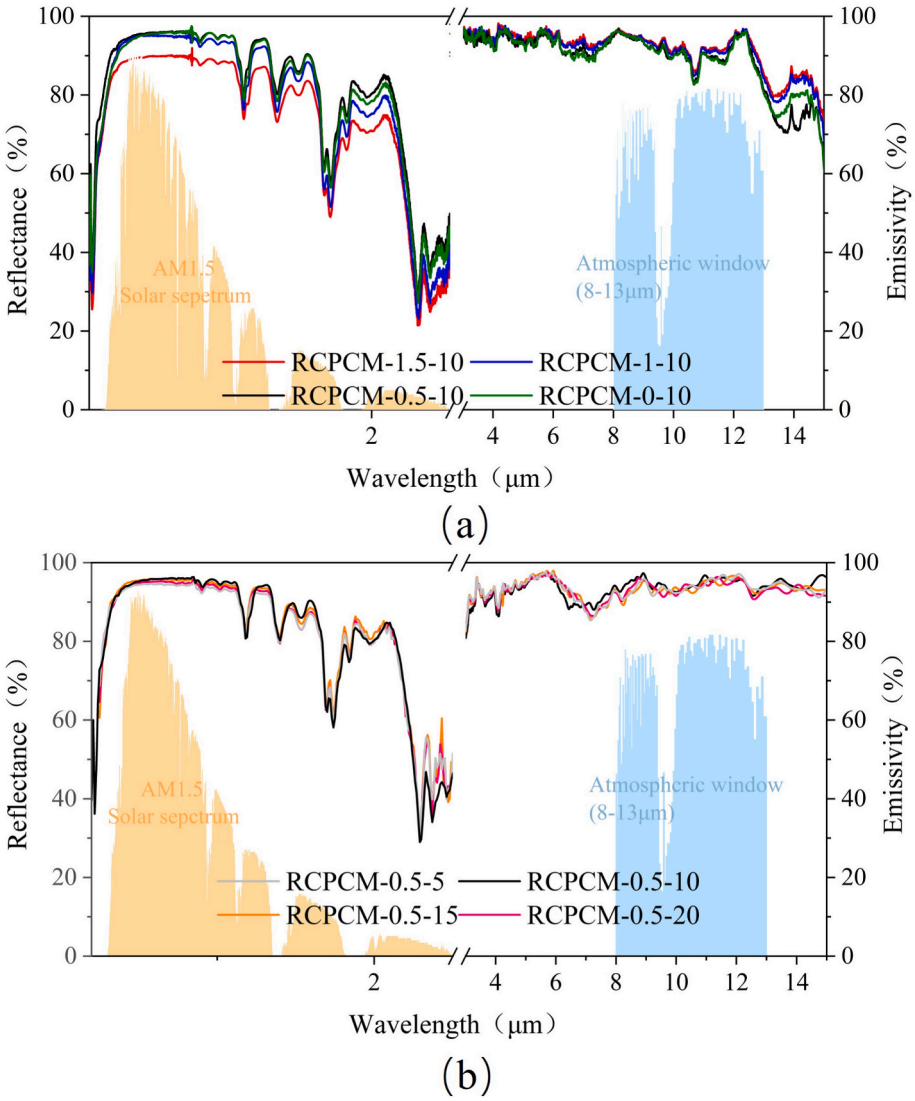

Fig. 6. RCPCM Solar Reflectance and Atmospheric Window Emissivity Curves. (a) Solar reflectance and atmospheric window emissivity spectra of RCPCM with varying radiative-cooling layer thickness ratios. (b) Solar reflectance and atmospheric window emissivity spectra of RCPCM with varying SiO_2 contents.

thus influence the quasi-steady surface temperature and ΔT. When the SiO_2 content is appropriate, it can regulate the mid-IR emissivity of the RC layer and at the same time keep the conductive heat losses at a relatively low level, which is beneficial to enhance the net radiative heat loss and reduce the steady-state temperature. However, increasing the SiO_2 content does not always lead to better cooling performance. Excessive SiO_2 may damage the microstructure and interfacial integrity of the bilayer RC layer, leading to poor adhesion between the PDMS/SiO_2 layer and the PDMS/h-BN layer and even inducing surface cracks or voids, which will increase parasitic non-radiative heat gains and weaken the effective radiative-cooling surface, thereby reducing the net cooling power.

To investigate the effect of PCM layer thickness on temperature control performance, RCPCM-0.5-10 samples were tested under a constant irradiance of 800 W/m^2, with results shown in Figs. 9(h) and 9(i). As the PCM thickness increases, the latent heat thermal energy storage capacity of the phase change layer improves, allowing it to absorb more heat during illumination. Consequently, the temperature rise rate of the samples under xenon lamp irradiation slows down, and the quasi-steady temperature during illumination is lower for thicker PCM layers. After 2 h of irradiation, the sample with an 8 mm PCM layer reaches the lowest temperature of only 32 °C, while the temperature gradually increases as the PCM thickness decreases. The sample with a 2 mm PCM layer reaches equilibrium in about 30 min, indicating that the PCM has largely completed its phase transition and the latent heat buffering effect is quickly exhausted; thereafter, temperature evolution is primarily governed by external heat exchange. In contrast, samples with PCM thicknesses of 4 mm, 6 mm, and 8 mm are still in the heating stage after 2 h, indicating ongoing heat absorption by the PCM. Fig. 9(i) further presents the temperature difference between RCPCM and the commercial coating ($\Delta T = T_{RCPCM} - T_{Commercial}$). During illumination, a thicker PCM generally corresponds to a lower ΔT, implying stronger cooling performance. After the xenon lamp is turned off, the heat stored in the PCM is gradually released, slowing the cooling rate and extending the thermal buffering time. Additionally, the temperature curves of the 6 mm and 8 mm samples almost overlap after illumination ceases, suggesting that further increasing PCM thickness offers limited improvement. This is because, after the light source is turned off, the PCM not only releases heat to the underside but also dissipates more heat to the environment through convection and thermal radiation. Overall, PCM thickness affects both temperature control during illumination and heat release behavior after the light source is turned off. Therefore, a thicker PCM layer is not always better; an appropriate thickness should be selected based on practical application requirements to achieve optimal overall

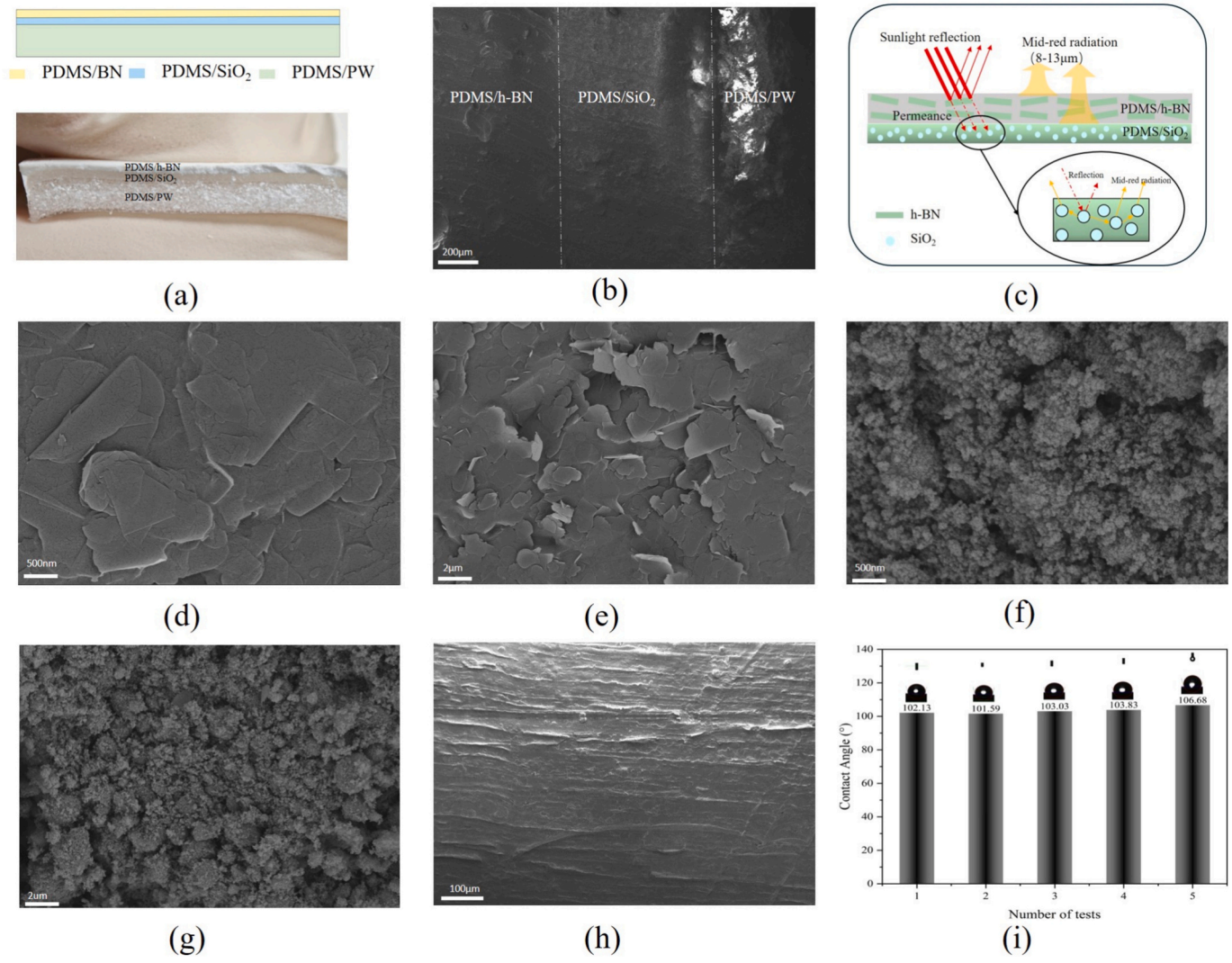

Fig. 7. SEM images of RCPCM structures and materials, and surface contact angle results (a) Schematic diagram of the three-layer structure of RCPCM radiative cooling and cross-section of RCPCM-0.5-10 sample (b) Cross-sectional SEM view of a three-layer structure (c) Radiation cooling principle diagram (d-e) SEM image of h-BN particles (f-g) SEM image of SiO_2 particles after ball milling. (h) Cross-sectional SEM view of a three-layer structure (i) RCPCM surface contact angle.

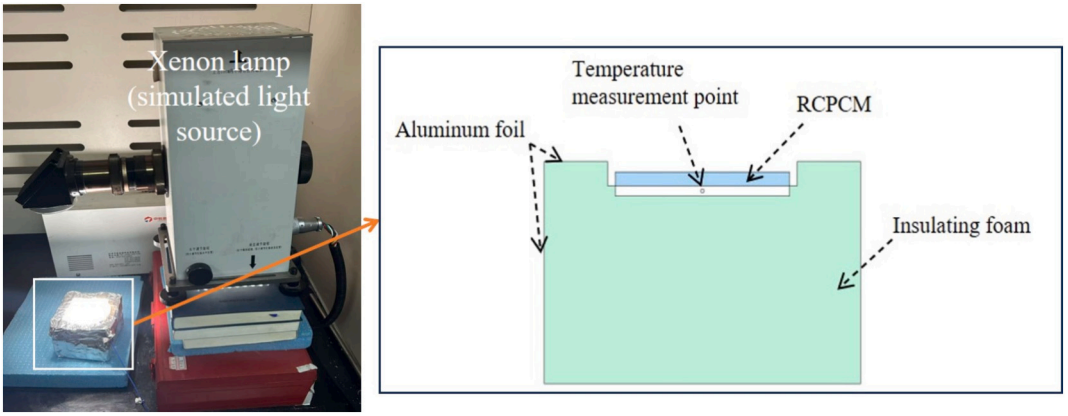

Fig. 8. Solar simulator and test apparatus.

performance.

3.3. Field RC performance of RCPCM

The all-day outdoor test was conducted in Chengdu, Sichuan, China (30.70°N, 104.06°E). The setup and results are shown in Fig. 10. As

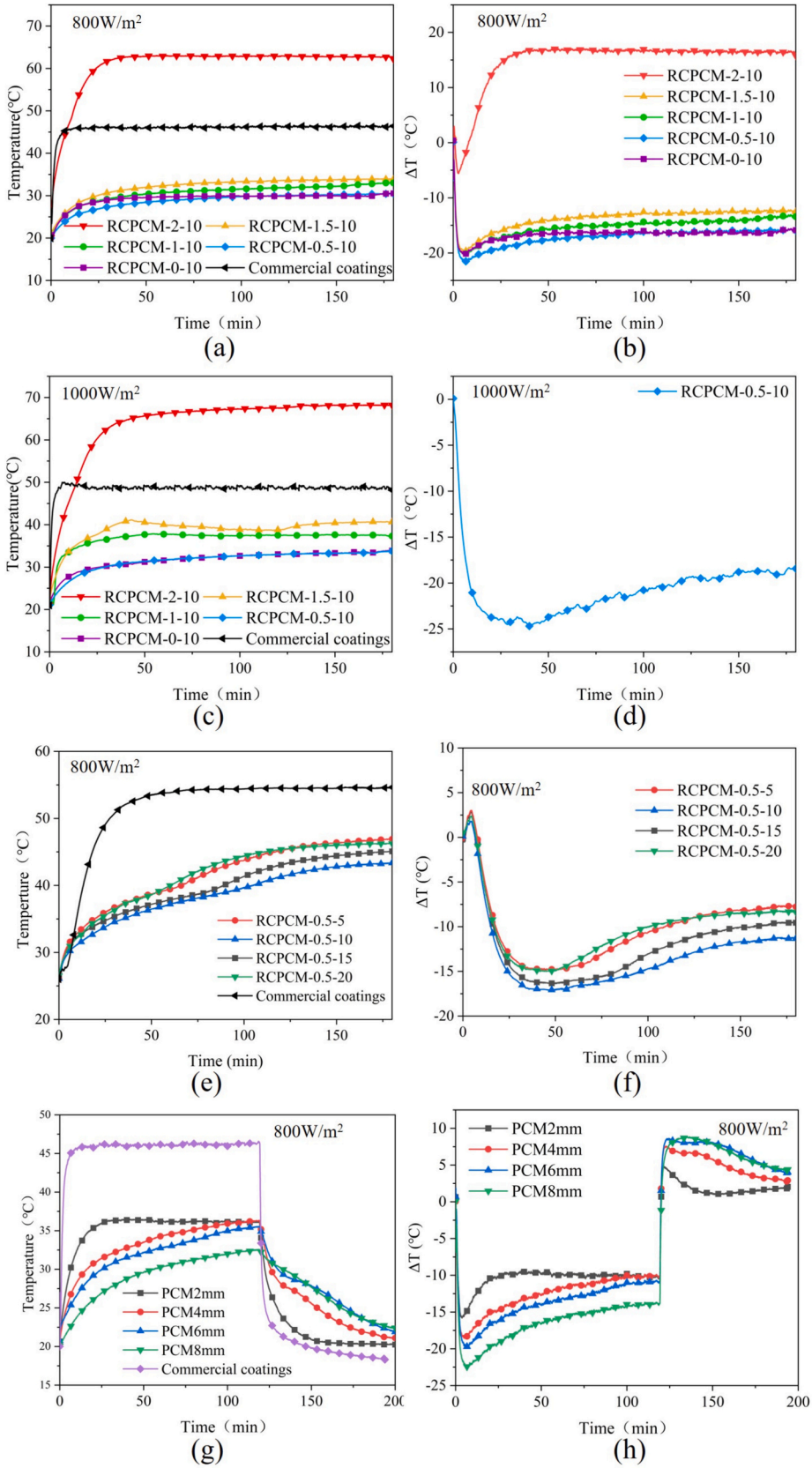

Fig. 9. Performance of the RCPCM under a solar simulator; (a) Performance of RCPCMs with different thickness ratios of the radiative-cooling layer at an irradiance of 800 W/m^2; (b) Temperature difference at 800 W/m^2 for RCPCM-1–5; (c) Performance of RCPCMs with different thickness ratios of the radiative-cooling layer at an irradiance of 1000 W/m^2; (d) Temperature difference at 1000 W/m^2; (e) Performance of RCPCMs with different SiO_2 contents at an irradiance of 800 W/m^2; (f) Temperature difference at 800 W/m^2 for RCPCMs with different SiO_2 contents; (g) Performance curves of materials with different PCM thicknesses under 800 W/m^2 light intensity; (h) Temperature differences between materials with different PCM thicknesses and commercial coatings under 800 W/m^2 light intensity.

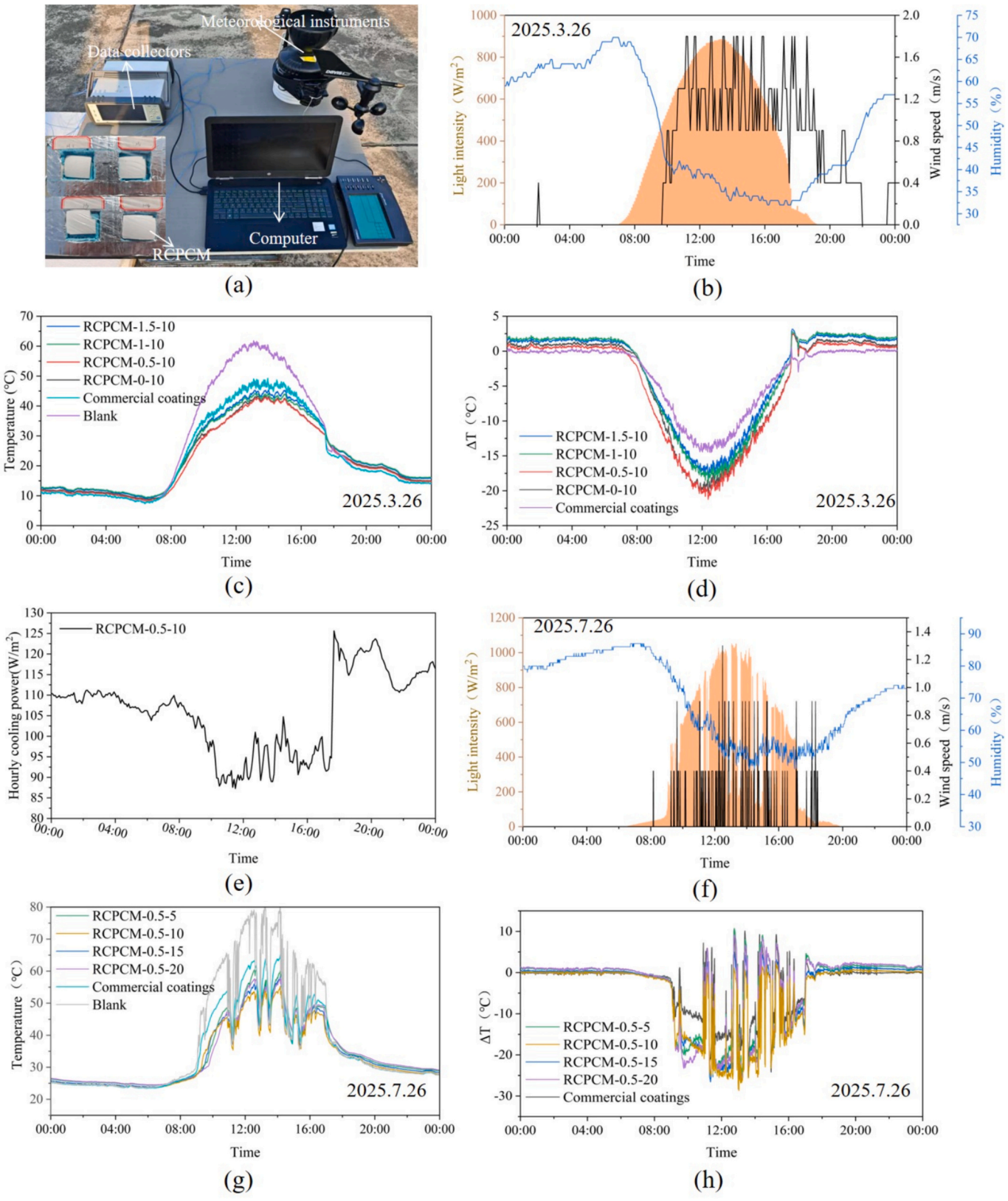

Fig. 10. Summer outdoor test results: (a) outdoor radiative-cooling performance test setup; (b) solar irradiance, wind speed, and humidity on the test day (2025.3.26); (c) temperature profiles of RCPCMs with different thickness ratios of the radiative-cooling layer; (d) temperature difference (ΔT) of RCPCMs with different radiative-cooling layer thickness ratios and the commercial coating relative to the blank cavity; (e) hourly radiative-cooling power of RCPCM-0.5-10; (f) solar irradiance, wind speed, and humidity on the test day (2025.7.26); (g) temperature profiles of RCPCMs with different SiO_2 contents; (h) temperature difference (ΔT) of RCPCMs with different SiO_2 contents and the commercial coating relative to the blank cavity.

shown in Fig. 10(c), the RCPCM provides cooling only from 08:00 to 17:30. After 17:30, solar irradiance decreases. The composite temperature drops rapidly. The PCM in the RCPCM begins to release energy stored during the day. Its temperature then becomes higher than that of the commercial coating and the blank cavity (T_{Blank}). From 08:00 to 17:30, the RC layer and PCM act synergistically, giving a larger temperature reduction for the RCPCM. After 17:30, PCM heat release raises the RCPCM temperature above the coating. After the PCM completes heat release, it still offers some thermal insulation and slows heat loss. The temperature thus remains higher than the coating and the cavity, which helps mitigate night-time overcooling. Fig. 10(d) gives $\Delta T = T - T_{Blank}$ for RCPCMs with different thickness ratios of the radiative-cooling layer. RCPCM-0.5-10 performs best, consistent with the solar-simulator results. Under a daytime peak irradiance of 880 W/m^2, RCPCM-0.5-10 reaches a maximum temperature drop of 21 °C and an average drop of 13.14 °C during 08:0017:30. The commercial coating shows only 14 °C maximum and 8.33 °C average over the same period. From 18:00 to 24:00, the temperature of RCPCM-0.5-10 is on average 0.82 °C above T_{Blank}. Fig. 10(g, h) present outdoor curves and ΔT for RCPCMs with different SiO_2 contents. RCPCM-0.5-10 shows the strongest cooling. Temperature fluctuations are evident due to unstable irradiance. During irradiance interruptions, ΔT becomes positive. RC weakens, the PCM stops charging and releases heat, and the temperature rises. After irradiance recovers, the RCPCM resumes cooling. The night-time heating effect weakens progressively because more PCM completes the liquid–solid transition and the ambient temperature falls. Fig. 10(e) reports the hourly radiative-cooling power of RCPCM-0.5-10 (March 26). Night-time power exceeds daytime power. In daytime, the film must handle both solar load and its own thermal radiation to space, which reduces net cooling. The all-weather power of RCPCM-0.5-10 exceeds 85 W/m^2. The maximum daytime power is 105 W/m^2. The maximum night-time power is 125 W/m^2.

As shown in Fig. 11, the winter outdoor radiative-cooling performance of RCPCM was tested in Chengdu on February 5, 2026. Under the winter condition, the temperature evolutions of RCPCM-0.5-10, the commercial coating and the blank reference are compared in Fig. 11(b). The temperature of the cavity rises the fastest, reaching a stable equilibrium of 30–33 °C. In contrast, both the commercial coating and RCPCM-0.5-10 effectively suppress the temperature rise. Throughout the daytime, RCPCM-0.5-10 maintains a temperature 2–4 °C lower than the commercial coating and remains significantly cooler than the cavity, indicating that its radiative cooling capability remains effective even in winter with reduced solar intensity. After sunset, as solar irradiance drops to zero and ambient temperature decreases, all samples cool down rapidly. However, RCPCM-0.5-10 exhibits a slower cooling rate and a higher nighttime equilibrium temperature compared to the commercial coating and cavity, indicating a clear thermal buffering effect of the PCM during the cooling stage. Fig. 11(c) further presents the temperature difference relative to the cavity (ΔT). During the day, all ΔT values are negative, meaning the surface temperatures are lower than that of the cavity. The minimum ΔT of RCPCM-0.5-10 ranges from −14 to −12 °C, while that of the commercial coating is about −10 to −8 °C, demonstrating the superior cooling effect of RCPCM-0.5-10. After sunset, ΔT gradually increases and turns positive as the stored energy is released from the PCM. The nighttime ΔT of RCPCM-0.5-10 reaches 2–3 °C, whereas that of the commercial coating remains negative or near zero. This is attributed to heat release from the PDMS/PW layer and reduced heat loss due to the multilayer structure. Overall, RCPCM-0.5-10 achieves both nighttime anti-overcooling and thermal buffering in winter, supporting its all-weather applicability and demonstrating the reliable multi-climate adaptability of the RCPCM design.

It is noteworthy that the results from the indoor solar simulator tests align with the outdoor roof measurements, with RCPCM-0.5-10 consistently demonstrating optimal performance under real meteorological conditions, thereby validating the reliability and engineering

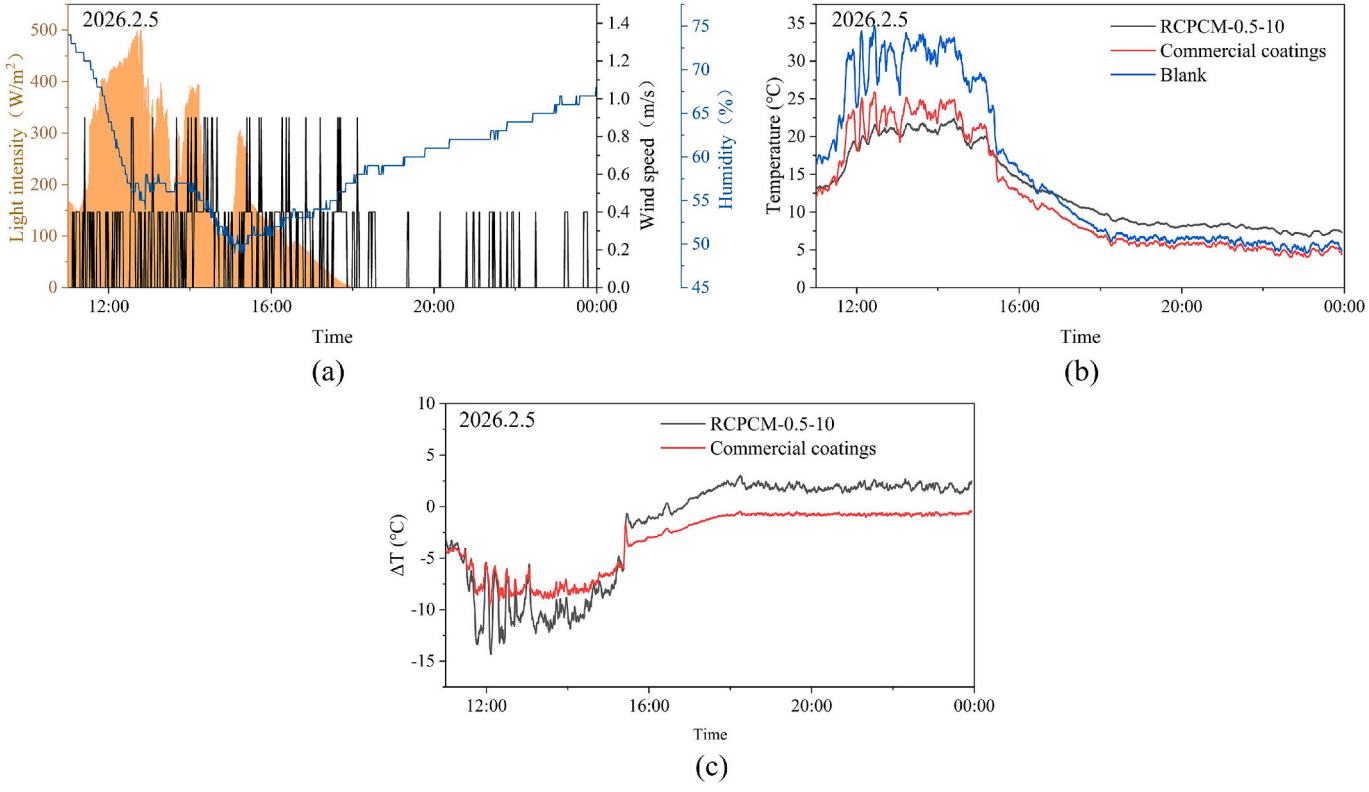

Fig. 11. Winter outdoor test results of RCPCM-0.5-10: (a) solar irradiance, wind speed, and humidity on the test day; (b) temperature profiles of the samples; (c) temperature difference (ΔT) of RCPCM-0.5-10 and the commercial coating relative to the blank cavity ($\Delta T = T - T_{Blank}$).

applicability of the structural design proposed in this study.

3.4. Comparison of RCPCM with reported studies

As shown in Fig. 12, the comparison between RCPCM and reported radiative-cooling-coupled phase-change composites is presented in terms of average solar reflectance and average emissivity. It can be observed that this work is located in the upper-right region of the scatter plot, indicating that RCPCM achieves both high average reflectance and high average emissivity simultaneously. Some reported RC-PCM systems enhance mid-infrared emission by introducing high-infrared polymers or porous emissive structures, but solar absorption or insufficient solar backscattering can reduce the average reflectance. Conversely, designs that maximize solar reflectance may sacrifice mid-infrared emissivity due to limited infrared-active thickness. In this study, the bilayer RC structure addresses this issue to some extent, where PDMS/h-BN provides strong solar backscattering to suppress solar heat gain, while PDMS/SiO_2 enables emissivity regulation within the atmospheric window. Consequently, RCPCM achieves an average solar reflectance of approximately 0.93 and an average emissivity of approximately 0.94, forming a more balanced optical-thermal combination and offering higher net radiative cooling potential under outdoor conditions. Compared with the trade-off between reflectance and emissivity observed in most reported studies, RCPCM achieves a superior match and balance between these two key optical parameters, thereby demonstrating a higher net radiative cooling potential outdoors. Therefore, the optimized optical performance of RCPCM helps maintain a lower surface temperature under solar irradiation and further enhances the applicability of radiative cooling in practical scenarios.

3.5. Energy saving performance of RCPCM

In order to reduce solar energy absorption, radiant cooling commercial coatings is able to achieve passive RC during the day, thus preventing excessive indoor temperatures during the daytime in summer. However, this can also lead to overcooling at night. In order to verify whether RCPCM-0.5-10 solves the problem of subcooling in different seasons and regions, Energy Plus was used to conduct energy simulations on buildings to investigate the potential energy savings of RCPCM-0.5-10. A model of a house with a total area of 96 m^2 in the double layer is shown in Fig. 11(a), where commercial coatings and RCPCM-0.5-10 are used as the outer layers of the walls. By operating the house in different regions, annual energy consumption results were obtained for each location, as shown in Fig. 13 and Table 8. Among the six cities, RCPCM achieved energy savings in five compared to traditional roofs, with only Lhasa showing an increase of 0.94 MJ/m^2 in energy savings per unit area. Compared to commercial coatings, RCPCM exhibited the lowest energy consumption in all cities, achieving additional savings ranging from 1.66 to 3.64 MJ/m^2. In summary, in eastern and southwestern cities where cooling demand dominates, RCPCM-0.5-10 delivers stable annual energy savings of 4–7 MJ/m^2. In severe cold and cold dry regions, it still maintains a modest net benefit of 1–2 MJ/m^2. Although a slight annual increase is observed in high-altitude cold cities, the system's performance remains comprehensively superior to that of commercial coatings.

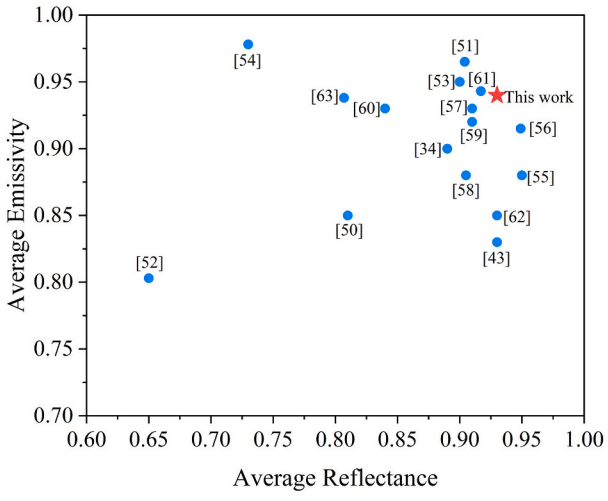

Fig. 12. Comparison of RCPCM with reported studies[34,43,50–63].

4. Conclusion

Although radiative cooling technology can dissipate heat to outer space, it is prone to nocturnal overcooling and ambient thermal shocks, limiting its benefits at the building scale. To address this issue, we designed and fabricated a trilayer radiative-cooling/phase-change composite membrane (RCPCM), which achieves efficient daytime cooling while suppressing nighttime temperature fluctuations. Optical characterization, xenon-lamp performance optimization, and outdoor field measurements were conducted on the RCPCM, and its building-level impacts were evaluated using EnergyPlus. The results are as follows:

(1) RCPCM exhibits excellent spectral selectivity-with an average solar reflectance of 0.93 (0.25–2.5 μm), a visible-band reflectance of 0.95, and an atmospheric-window emissivity of 0.94-indicating its strong potential for radiative cooling.
(2) The optimal thicknesses of the radiative cooling layers are 1.5 mm (PDMS/h-BN layer) and 0.5 mm (PDMS/SiO_2 layer); cooling performance improves as the SiO_2 content increases to 10 wt% but declines thereafter. Increasing the thickness of the phase change material layer delays the surface rewarming phenomenon after the cessation of irradiation, with similar thermal equilibrium behavior observed at thicknesses of 6 mm and 8 mm.
(3) In outdoor tests, the RCPCM-0.5-10 configuration achieved a maximum daytime temperature reduction of 22 °C compared to the reference cavity during summer, with peak cooling powers of 125 W/m^2, while avoiding excessive nocturnal overcooling. During winter nights, it exhibited a temperature increase of 0–3°C compared to the cavity and commercial coatings, indicating that RCPCM-0.5-10 can also mitigate overcooling issues in winter, demonstrating the all-season applicability of RCPCM.
(4) EnergyPlus simulations further validate the effectiveness of RCPCM in reducing summer cooling loads and improving winter heating efficiency. In eastern and southwestern cities where cooling demand dominates, RCPCM achieves energy savings of 4–7 MJ/m^2. In severe cold and cold dry regions, it still maintains savings of 1–2 MJ/m^2. Although a slight increase in energy consumption is observed in high-altitude cold climate zones, its performance remains superior to that of commercial coatings, effectively mitigating the risk of overcooling.

Overall, coupling a high-selectivity radiative surface with latent-heat storage provides a practical, low-energy pathway to climate-adaptive building envelopes that reduce heating/cooling demand and stabilize indoor thermal conditions.

CRediT authorship contribution statement

Hengkang He: Writing – review & editing. **Qingyun Zhao:** Writing – review & editing. **Bozhong Chen:** Writing – review & editing. **Zhaoli Zhang:** Writing – review & editing. **Nan Zhang:** Writing – review & editing. **Shady Attia:** Writing – review & editing. **Yanping Yuan:** Writing – review & editing. **Jerzy Wołoszyn:** Writing – review & editing.

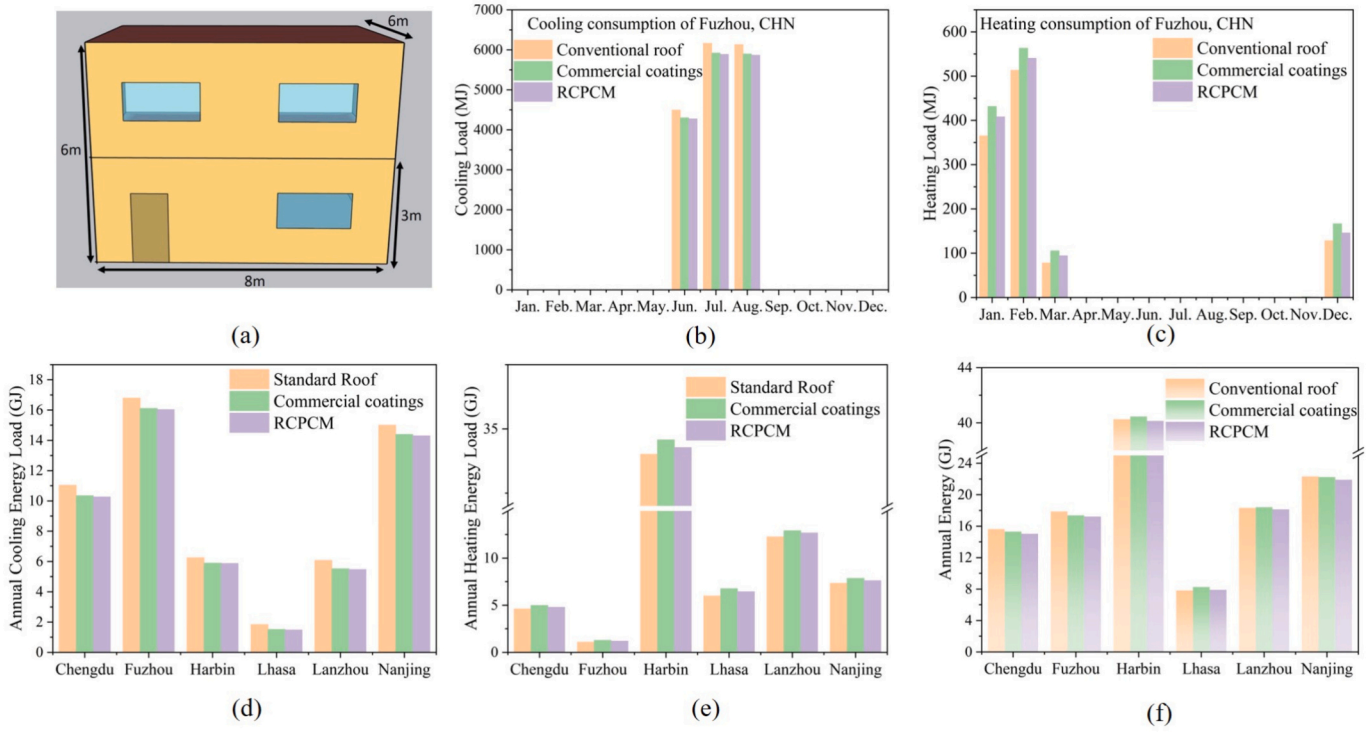

Fig. 13. Energy saving analysis of RCPCM-0.5-10 (a) Building model in Energy Plus, (b) Comparison of cooling loads for conventional roofs, commercial coatings, and RCPCM in Fuzhou, China, (c) Comparison of heating loads for conventional roofs, commercial coatings, and RCPCM in Fuzhou, China, (d) Comparison of annual cooling loads of RCPCM, commercial coatings, and conventional roofs in six typical Chinese cities, (e) Comparison of annual heating loads of RCPCM, commercial coatings, and conventional roofs in six typical Chinese cities, (f) Comparison of annual energy of RCPCM, commercial coatings, and conventional roofs in six typical Chinese cities.

Table 8
Energy Per Conditioned Building Area and Energy Savings Conditioned Building Area.

	Energy Per Conditioned Building Area (MJ/m^2)			Energy Savings Conditioned Building Area (MJ/m^2)	
	Conventional roof	Commercial coating	RCPCM	Commercial coating	RCPCM
Chengdu	162.81	159.48	156.67	3.33	6.14
Fuzhou	186.15	181.04	179.38	5.11	6.77
Harbin	419.38	421.46	418.13	−2.08	1.25
Lhasa	81.46	86.04	82.40	−4.58	−0.94
Lanzhou	190.83	191.88	188.96	−1.05	1.87
Nanjing	232.60	231.67	228.23	0.93	4.37

Declaration of competing interest

The authors declare that they have no known competing financial interests or personal relationships that could have appeared to influence the work reported in this paper.

Acknowledgments

This work was supported by the National Natural Science Foundation of China (No. 52378111).

Data availability

Data will be made available on request.

References

[1] Steven C. Sherwood, Adapting to the challenges of warming, Science 370 (6518) (2020) 782–783.
[2] Elizabeth Pennisi, Living with heat, Science 370 (6518) (2020) 778–781.
[3] Oliver Inderwildi, Chuan Zhang, Xiaonan Wang, et al., The impact of intelligent cyber-physical systems on the decarbonization of energy, Energy Environ. Sci. 13 (3) (2020) 744–771.
[4] Putla Sudarsanam, Ruyi Zhong, Sander Van den Bosch, et al., Functionalised heterogeneous catalysts for sustainable biomass valorisation, Chem. Soc. Rev. 47 (22) (2018) 8349–8402.
[5] Yi Wang, Haining Ji, Jiamei Huang, et al., A metasurface-integrated multilayer solar reflector design for daytime radiative cooling, Appl. Therm. Eng. 278 (2025) (Part A): 127431.
[6] Yanping Yuan, Xiangkui Gao, Hongwei Wu, et al., Coupled cooling method and application of latent heat thermal energy storage combined with pre-cooling of envelope: method and model development, Energy 119 (2017) 817–833.
[7] Weiguang Su, Pei Cai, Jo Darkwa, et al., Review of daytime radiative cooling technologies and control methods, Appl. Therm. Eng. 235 (2023) 121305.
[8] Ning Yang, Sizhe Xue, Muhammad Riaz Ahmad, et al., Development of red mud-modified geopolymer coating with radiative cooling effect for footway application, J. Clean. Prod. 450 (2024) 141915.
[9] Xinpeng Zhao, Tangyuan Li, Hua Xie, et al., A solution-processed radiative cooling glass, Science 382 (6671) (2023) 684–691.
[10] Yi Wang, Haining Ji, Bin Liu, et al., Radiative cooling: structure design and application, J. Mater. Chem. A 12 (2024) 9962–9978.
[11] Sajith Wijesuriya, Ravi Anant Kishore, Marcus V.A. Bianchi, et al., Potential energy savings benefits and limitations of radiative cooling coatings for u. s. a. residential buildings, J. Clean. Prod. 379 (2022) (Part 2): 134763.
[12] Lufang Chen, Kai Zhang, Mingquan Ma, et al., Sub-ambient radiative cooling and its application in buildings, Build. Simul. 13 (2020) 1165–1189.
[13] Xiangshun Li, Huilin Xu, Yuchen Yang, et al., Selective spectral absorption of nanofibers for color-preserving daytime radiative cooling, Mater. Horiz. 10 (7) (2023) 2487–2495.
[14] Po-Chun Hsu, Alex Y. Song, Peter B. Catrysse, et al., Radiative human body cooling by nanoporous polyethylene textile, Science 353 (6303) (2016) 1019–1023.
[15] Wei Li, Yu Shi, Kaifeng Chen, et al., A comprehensive photonic approach for solar cell cooling, ACS Photonics 4 (4) (2017) 774–782.
[16] Huanzheng Zhu, Qiang Li, Chenning Tao, Multispectral camouflage for infrared, visible, lasers and microwave with radiative cooling, Nat. Commun. 12 (2021) 1805.

[17] Masamichi Kobayashi, Kohji Tashiro, Hiroyuki Tadokoro, Molecular vibrations of three crystal forms of poly(vinylidene fluoride), Macromolecules 8 (1975) 158–171.
[18] Minwoo Choi, Junyong Seo, Siwon Yoon, et al., All-day radiative cooling using a grating-patterned PDMS film emitter, Appl. Therm. Eng. 214 (2022) 118771.
[19] Xiaoning Zhang, Jun Qiu, Junming Zhao, et al., Complex refractive indices measurements of polymers in infrared bands, J. Quant. Spectrosc. Radiat. Transf. 252 (2020) 107063.
[20] Yubo Zhang, Xinyu Tan, Guiguang Qi, et al., Effective radiative cooling with ZrO_2/PDMS reflective coating, Sol. Energy Mater. Sol. Cells 229 (2021) 111129.
[21] Xiongbo Yang, Jialin Geng, Xinyu Tan, et al., A flexible PDMS@ZrO_2 film for highly efficient passive radiative cooling, Inorg. Chem. Commun. 151 (2023) 110586.
[22] Junbo Jung, Siwon Yoon, Bumjoo Kim, et al., Development of high-performance flexible radiative cooling film using PDMS/TiO2 microparticles, Micromachines 14 (12) (2023) 2223.
[23] Pragathi Pandian, Palanichamy Sundaram, Anbalagan Sathishkumar, et al., Effect of sodium dodecyl sulfate surfactant on the surface properties of electroless NiP-TiO2-ZrO2 composite coatings on magnesium AZ91D substrate, Arab. J. Chem. 16 (2023) 105028.
[24] Tao Li, Haoyang Sun, Meng Yang, et al., All-ceramic, compressible and scalable nanofibrous aerogels for subambient daytime radiative cooling, Chem. Eng. J. 452 (4) (2022) 139518.
[25] Rong Chen, Huiyu Yang, Xiaohua Cheng, et al., Natural silk nanofiber aerogel/SiO_2 microsphere composite film with unique hierarchical structure for thermal insulation and high-performance radiative cooling, Ind. Crop. Prod. 221 (2024) 119388.
[26] Chaohua Xue, Renxuan Wei, Xiaojing Guo, et al., Fabrication of superhydrophobic P(VDF-HFP)/SiO_2 composite film for stable radiative cooling, Compos. Sci. Technol. 220 (2022) 109279.
[27] Junghwan Lee, Dohyun Im, Sohyeon Sung, et al., Scalable and efficient radiative cooling coatings using uniform-hollow silica spheres, Appl. Therm. Eng. 254 (2024) 123810.
[28] Zhilong Lin, Lingshan Miao, Huanji Song, et al., Rod-like boron nitride based-coating for subambient and above-ambient passive radiative cooling, Appl. Surf. Sci. 689 (2025) 162502.
[29] Juncheng Xia, Xiangdong Kong, Linhong Li, et al., High thermal conductivity and radiative cooling designed boron nitride Nanosheets/silk fibroin films for personal thermal management, ACS Appl. Mater. Interfaces 16 (6) (2024) 7732–7741.
[30] Yuting Fu, Le Chen, Yuao Guo, et al., Pyramid textured photonic films with high-refractive index fillers for efficient radiative cooling, Adv. Sci. 11 (39) (2024) 2404900.
[31] Satoshi Ishii, Etsuko Shimada, Ryugo Hosokawa, et al., Double-layer coating containing boron nitride powder for efficient daytime radiative cooling, ACS Appl. Opt. Mater. 3 (3) (2025) 720–726.
[32] Armande Hervé, Jérémie Drévillon, Younès Ezzahri, et al., Radiative cooling by tailoring surfaces with microstructures: association of a grating and a multi-layer structure, J. Quant. Spectrosc. Radiat. Transf. 221 (2018) 155–163.
[33] Qi Wang, Haitao Yu, Junhui Fan, et al., Passive daytime radiative cooling composite films with super-amphiphobic, friction-resistant and flame-retardant properties, Mater. Lett. 366 (2024) 136515.
[34] Xuying Liu, Zhixuan Fan, Xiongjin Cao, et al., Comprehensive performance of a novel radiative cooling phase change roof: an experimental study, Appl. Therm. Eng. 243 (2024) 122568.
[35] Dongmei Shen, Cairui Yu, Wanfen Wang, Investigation on the thermal performance of the novel phase change materials wall with radiative cooling, Appl. Therm. Eng. 176 (2020) 115479.
[36] Waseem Aftab, Ali Usman, Jinming Shi, et al., Phase change material-integrated latent heat storage systems for sustainable energy solutions, Energy Environ. Sci. 14 (2021) 4268–4291.
[37] A. Sathishkumar, P. Sundaram, K.S. Vignesh, et al., Solidification characteristics of biomass-activated aloe vera PCM in a spherical enclosure for efficient cool thermal energy storage, Case Stud. Therm. Eng. 75 (2025) 106362.
[38] A. Sathishkumar, P. Sundaram, Rajendran Prabakaran, et al., Graphene based fatty acid phase change material as an alternative to water: an experimental investigation on thermal energy storage characteristics, Colloids Surf. A Physicochem. Eng. Asp. 715 (2025) 136589.
[39] A. Sathishkumar, P. Sundaram, S. Praveen Ranga, et al., Role of *aloe vera* based nanofluids for cool thermal energy storage system: a comparative study, J. Energy Storage 90 (2024) (Part A): 111710.
[40] Meng Yang, Hongmei Zhong, Tao Li, et al., Phase change material enhanced radiative cooler for temperature-adaptive thermal regulation, ACS Nano 17 (2) (2023) 1693–1700.
[41] Mulin Qin, Kaihang Jia, Ali Usman, et al., High-efficiency thermal-shock resistance enabled by radiative cooling and latent heat storage, Adv. Mater. 36 (25) (2024) 2314130.
[42] Siqi Wang, Minqiang Wu, Han Han, et al., Regulating cold energy from the universe by bifunctional phase change materials for sustainable cooling, Adv. Energy Mater. 14 (45) (2024) 2402667.
[43] Shuang Tao, Qizhong Wan, Ying Xu, et al., Incorporation form-stable phase change material with passive radiative cooling emitter for thermal regulation, Energ. Buildings 288 (2023) 113031.
[44] Mulin Qin, Feng Xiong, Waseem Aftab, et al., Phase-change materials reinforced intelligent paint for efficient daytime radiative cooling, iScience 25 (7) (2022) 104584.
[45] S. Jellaj, S. Ouhaibi, L. Zahiri, et al., Phase change materials and building envelope: an innovative solution for energy transition, Curr. Appl. Phys. 80 (2025) 82–98.
[46] Pengli Li, Ao Wang, Junjie Fan, et al., Thermo-optically designed scalable photonic films with high thermal conductivity for subambient and above-ambient radiative cooling, Adv. Funct. Mater. 32 (5) (2021) 2109542.
[47] Jie Qin, Zihan Zhang, Yanwen Li, et al., Design and manufacture of a radiative cooler to measure the subambient cooling effect and cooling power, Rev. Sci. Instrum. 93 (2022) 054901.
[48] Paulo Cesar Tabares-Velasco, Craig Christensen, Marcus Bianchi, Verification and validation of EnergyPlus phase change material model for opaque wall assemblies, Build. Environ. 54 (2012) 186–196.
[49] Kyoung Ok Lee, Mario A. Medina, Xiaoqin Sun, Development and verification of an EnergyPlus-based algorithm to predict heat transfer through building walls integrated with phase change materials, J. Build. Phys. 40 (1) (2016) 77–95.
[50] Yuruo Zhang, Xianghui Liu, Zhenyang Li, et al., Colourful phase change material-incorporated flexible film for efficient passive radiative cooling, Nanotechnology 34 (41) (2023) 415702.
[51] Bo Xiang, Peng Xu, Renzhi Li, et al., Phase change material-based film toward enhanced radiative cooling and mitigation of overcooling, ACS Appl. Polym. Mater. 6 (1) (2023) 515–523.
[52] Luyao Yang, Changping Feng, Lu Bai, et al., Flexible shape-stabilized phase change materials with passive radiative cooling capability for thermal management, Chem. Eng. J. 425 (2021) 131466.
[53] Bin Gu, Zhaofeng Dai, Haodan Pan, et al., Integration of prolonged phase-change thermal storage material and radiative cooling textile for personal thermal management, Chem. Eng. J. 493 (2024) 152637.
[54] Zilin Yu, Fang Wang, Wenqing He, et al., Phase-change material-integrated dual-mode thermal management janus films with enhanced radiative cooling and solar heating, ACS Appl. Polym. Mater. 7 (6) (2025) 3555–3563.
[55] Zhijun Zhu, Akbar Bashir, Xiaohong Wu, et al., Highly integrated phase change and radiative cooling fiber membrane for adaptive personal thermal regulation, Adv. Funct. Mater. 35 (2025) 2416111.
[56] Yuanxiang Xiao, Zhi Chen, Weishi Zheng, et al., A janus fabric composed of temperature-adaptive phase-changing and radiative cooling layers for dynamic personal thermal management, Chem. Eng. J. 521 (2025) 166795.
[57] Wanwan Li, Tong Yang, Xinwei Dong, et al., Dual-mode passive thermal management for outdoor electrical houses based on the coupling of phase change thermal storage and radiative cooling, Case Stud. Therm. Eng. 77 (2026) 107482.
[58] Wentao Zhang, Xingchi Jiang, Zhu Cheng, et al., High-performance thermal management materials: synergistic integration of passive radiative cooling and latent heat storage capabilities, Energy Convers. Manag. 344 (2025) 120301.
[59] Xiangfei Kong, Baochun Cui, Yongkang Zhao, et al., A novel flexible dual-mode phase change material for year-round energy saving, J. Energy Storage 124 (2025) 116912.
[60] Zhenyu Zhang, Haosen Ma, Yu He, et al., High reflectivity and latent heat synergetic TiO_2/$Cs_{0.33}WO_3$-PU double-layer materials with zero transmittance, Chem. Eng. J. 496 (2024) 154104.
[61] Ziqi Li, Akbar Bashir, Chak Yin Tang, et al., Thermochromic radiative cooling coatings with robust superhydrophobicity for energy-efficient buildings, Energy Environ. Mater. 9 (2026) e70278.
[62] Kun Yang, Ziyu Huo, Na Du, et al., Experimental investigation of the performance of an innovative delignified wood-based phase change roof integrated with sky radiation cooling, Energy 325 (2025) 136163.
[63] Peimin Wang, Mulin Qin, Kaihang Jia, et al., High-efficiency and scalable cooling solution for parked cars: coupling radiative cooling and latent heat storage, ACS Mater. Lett. 7 (6) (2025) 2213–2220.